J. Fluid Mech. (1988), *vol.* 189, *pp.* 423–442
Printed in Great Britain

Deep-water plunging breakers: a comparison between potential theory and experiments

By DOUGLAS G. DOMMERMUTH, DICK K. P. YUE, W. M. LIN, R. J. RAPP

Department of Ocean Engineering, Massachusetts Institute of Technology, Cambridge, MA 02139, USA

E. S. CHAN AND W. K. MELVILLE

Department of Civil Engineering, Massachusetts Institute of Technology, Cambridge, MA 02139, USA

(Received 9 March 1987)

The primary objective of this paper is to provide a *detailed* confirmation of the validity of potential-flow theory for describing steep gravity waves produced in an experimental tank. Very high-resolution computations are carried out which use a refined mixed Eulerian–Lagrangian solution scheme under the assumptions of potential flow. The numerical results for a plunging breaker produced by a programmed piston-type wavemaker are found to be in excellent agreement with tank measurements up to and including overturning. The calculated free-surface elevations are almost indistinguishable from measured profiles, even close to where the wave plunges. The horizontal and vertical water-particle velocities measured with a laser anemometer throughout the water depth at two longitudinal stations are also well predicted by the theory. In contrast to the fully nonlinear theory, predictions based on linearized theory become poorer as the wave packet moves down the tank. To allow other investigators to evaluate the computations and experiments, the Fourier amplitudes and phases which completely specify the time history of the wavemaker's velocity are given in Appendix B.

1. Introduction

Ever since the work of Ursell, Dean & Yu (1959), who compared the waves created by a piston wavemaker to theoretical predictions based on linearized equations, the validity and limitations of classical small-amplitude wave theory have been well established. In particular, they found that for small wave steepness, $H/\lambda \leqslant 0.03$, (wave height H, wavelength λ), the error in the wave height in front of the wavemaker is of the order of 3%, although for steeper waves ($0.045 \leqslant H/\lambda \leqslant 0.048$) the deviations, presumably primarily due to nonlinearity, can be as much as 10%.

In the present work, we aim to verify against carefully controlled experiments in a wave tank the validity of fully nonlinear potential-flow theory for steep gravity waves up to and including overturning. Surface tension is ignored. Specifically, we consider the problem of a single plunging breaker created downstream of a piston wavemaker. The breaking wave is produced by generating a spectrum of waves whose phases are adjusted so that their superposition gives rise to a rapid increase

in wave amplitude a prescribed distance away from the wavemaker (Longuet-Higgins 1974; Greenhow *et al.* 1982).

This research is motivated by recent experimental work on breaking waves (Chan 1985; Melville & Rapp 1985; Rapp 1986), and the successful application of the mixed Eulerian–Lagrangian method of Longuet-Higgins & Cokelet (1976) to the study of two-dimensional periodic breaking waves. In many of the investigations to date (e.g. Vinje & Brevig 1981; New, McIver & Peregrine 1985), improvements of the method have been developed for studying spatially periodic waves but with no surface-piercing boundaries.

At the intersection of a body with a free surface, i.e. the contact point, there exists a weak singularity due to the confluence of boundary conditions. This has been studied by several authors, and is reviewed, for example, by Dommermuth & Yue (1987). For a wavemaker started impulsively, D. H. Peregrine (1972, unpublished notes) showed that to leading order in a small-time expansion the surface elevation behaves like $t \log(\tanh(\pi x/4h))$, where t is time, $x\,(x > 0)$ is the horizontal distance measured from the wavemaker, and h is the water depth. Lin (1984), who considered the nonlinear wavemaker problem, proposed an effective numerical treatment at the contact point and obtained results *near* the wavemaker which confirmed Peregrine's leading-order solution, and which also agreed well with experiments for both impulsively started and sinusoidally driven pistons. Significantly, Lin's approach eliminated the need for extrapolation (Vinje & Brevig 1981) or even experimental input (Greenhow *et al.* 1982) to fix the locations of the intersection points to obtain acceptable results.

In almost all these numerical studies, high-wavenumber instabilities of the free surface occurred unless special treatment such as smoothing was used. Following Fink & Soh (1974), Dommermuth & Yue (1987) in their studies of the nonlinear axisymmetric waves implemented a regridding algorithm which effectively removed the instabilities without causing additional problems at the intersection points which smoothing did.

In the present numerical simulation, we adopt many of these developments in a refined semi-Lagrangian scheme which uses the Cauchy-integral formulation of Vinje & Brevig (1981), the wavemaker and free-surface intersection-point treatment of Lin, Newman & Yue (1984), and the regridding idea of Dommermuth & Yue (1987). Like Longuet-Higgins & Cokelet (1976), a dynamically controlled time-stepping procedure is used to capture the large accelerations in the breaking wave. A high-resolution computation is then performed using only the displacement of the wavemaker in the experiment as input. The numerical simulation compares extremely well with the experimental measurements for the free-surface elevations, and the horizontal and vertical velocities below and above the still-water level. These comparisons confirm the validity and usefulness of such nonlinear potential-flow computations for predicting overturning waves (up to re-entry) and surface jets in the ocean environment.

After establishing the accuracy of the numerical simulation, several interesting results not readily measurable from the wave tank such as the work done by the wavemaker, the energy in the fluid, and the velocities and accelerations of free-surface particles in the plunging jet are studied to illustrate salient features of the deep-water breaking wave.

Section 2 describes the experimental set-up and measurements for breaking waves in a tank, §3 gives a short summary of the mixed Eulerian–Lagrangian formulation for fully nonlinear potential flow, and §4 details the numerical implementation.

Extensive comparisons between the experiments and computations for the case of a single plunging wave are given in §5 which also contains other computed results for the breaking wave.

2. Experiments

The experiments are conducted at the Ralph M. Parsons Laboratory of MIT in a glass-walled channel 25 m long, 0.7 m wide, filled to a depth of 0.6 m with fresh water. A wooden beach of slope 0.1 covered with 5 cm thick fibrous mats dissipates the waves at the far end of the tank so that less than 4% of the incident-wave amplitude is reflected. The beach toe is 19.5 m from the rest position of the paddle and extends to 25 m at the waterline. Measurements are completed before the most energetic wave frequencies are reflected back to the measurement point, thus further reducing the influence of reflections.

The channel is equipped with a servo-controlled, hydraulically activated wavemaker driven under program control. The hydraulic cylinder moves a rigid vertical bulkhead horizontally, so that the velocity at the paddle is uniform with depth. The paddle is supported on springs and sealed on the sides and bottom with rubber wipers. The input to the wavemaker is computed taking account of the transfer function of the entire wave-generator system. For these experiments, the input to the wavemaker is thirty-two equally spaced components in the range 0.56–1.2 Hz. The spectrum is flat except at the ends where it is tapered to zero, and the phases are chosen according to linear theory such that they are the same at a prescribed point down the channel.

The free-surface displacement is measured with a set of surface-piercing resistance-wire wave gauges, attached to Danish Hydraulic Institute (model 80-74G) a.c. bridges. The complete wave-gauge system has a resolution of $O(0.01$ cm). Simultaneous horizontal and vertical fluid velocity components are measured with a laser anemometer operating in the dual-beam backscatter mode with counter data processors. The system uses a LEXEL 95-2 argon-ion laser and ThermoSystems Inc. optics which is functionally equivalent to the TSI model 9100-7 laser-anemometer system. The water in the channel is seeded with silicon carbide particles of 1.5 μm mean diameter. Measurements are taken through the glass sidewall of the channel, with the measuring volume well outside the sidewall boundary layer. Typical r.m.s. noise levels for the velocity measurements are $O(0.1$ cm/s).

The 'top-hat' spectrum to the wavemaker is characterized by three dimensionless parameters measuring the amplitude, bandwidth and phase (Melville & Rapp 1985) scaled with the centre frequency. It is found that the strength of breaking is most sensitive to changes in the amplitude parameter (Chan 1985; Rapp 1986) and in these experiments it is chosen to give a single plunging wave. The wave plunges, that is the forward face touches the forward trough, at approximately 7.25 m from the paddle at a time approximately 12.9 s from the paddle start. The wave gauges are positioned at $x = 1.9$, 3.0, 4.0, 5.0, 5.5, 6.0, 6.5, 7.1 and 7.3 m (see figure 3*a*). The velocities are measured at $x = 3.0$ and 5.0 m from near the bottom of the tank to above the still-water level. Measurements are obtained from repeated runs of the experiment, which is repeatable to within 0.01 s over the duration, and to within ± 2 cm horizontally over the distance to breaking. Complete details of the experimental procedure can be found in Chan (1985) and Rapp (1986).

3. Mathematical formulation

The mathematical formulation we use is similar to Vinje & Brevig (1981) and is outlined here for completeness. The physical problem is formulated as the irrotational flow of an homogeneous, incompressible, and inviscid fluid in a two-dimensional rectangular tank of length $L(t)$ with a vertical piston wavemaker at one end. Surface tension is not considered. We define Cartesian coordinates with the origin at the intersection of the undisturbed water surface ($y = 0$) and at the rest position of the wavemaker ($x = 0$), with y positive up. For simplicity, the units of length, time, and mass are chosen so that the initial depth of the water, the gravitational acceleration, and the fluid density are all unity. We define the complex potential

$$\beta(z,t) = \phi(x,y,t) + \mathrm{i}\psi(x,y,t), \tag{3.1}$$

where $z = x + \mathrm{i}y$. Since both the velocity potential ϕ and the stream function ψ are solutions to Laplace's equation in the fluid domain, the Cauchy integral theorem can be applied to give

$$2\pi\mathrm{i}\,\beta(\zeta,t) = \int_C \frac{\beta(z,t)}{z-\zeta}\,\mathrm{d}z, \tag{3.2}$$

where the contour of integration, $C(z,t)$, is a closed path which includes the wavemaker B, the free surface F, the far end of the tank ($x = L$) B_L, and the bottom ($y = -1$) B_0; and ζ is inside C. On the wavemaker, which is vertical, the horizontal velocity $U(t)$ is prescribed and the stream function is given by

$$\psi = U(t)\,(y+1) \quad \text{on } B(x,t). \tag{3.3}$$

Similarly, on the bottom and the vertical wall at the end of the tank the condition of no normal flux gives

$$\psi = 0 \quad \text{on } B_0, B_L. \tag{3.4}$$

On the free surface, the kinematic boundary condition can be written as

$$\frac{\mathrm{D}z}{\mathrm{D}t} = \frac{\partial\beta^*}{\partial z} \quad \text{on } F(z,t), \tag{3.5a}$$

where $\mathrm{D}/\mathrm{D}t \equiv \partial/\partial t + \nabla\phi\cdot\nabla$ is the material derivative, and an asterisk denotes a complex conjugate. From Bernoulli's equation, the dynamic boundary condition for zero atmospheric pressure on the free surface gives

$$\frac{\mathrm{D}\phi}{\mathrm{D}t} = \frac{1}{2}\left|\frac{\partial\beta}{\partial z}\right|^2 - y \quad \text{on } F(z,t). \tag{3.5b}$$

With the specification of initial conditions corresponding to the fluid being at rest at $t = 0$, the initial-boundary-value problem for $\beta(z,t)$ (and $F(z,t)$) is complete. We solve the system using a mixed Eulerian–Lagrangian method (Longuet-Higgins & Cokelet 1976). At any instant of time t, the wavemaker position $B(x,t)$ and the stream function $\psi(z,t)$ on B, B_0 and B_L are prescribed, and the free-surface elevation $F(z,t)$ and the velocity potential $\phi(z,t)$ on it are given from integration of the evolution equations (3.5). Equation (3.2) is used to solve for the unknown $\phi(z,t)$ on B, B_0 and B_L, and $\psi(z,t)$ on F. As a result, we can integrate (3.5) for the new Lagrangian value of $\phi(z,t+\Delta t)$ on the free surface and its position $F(z,t+\Delta t)$ and the whole process is repeated.

To minimize the final number of unknowns, we can take advantage of the fact that ϕ is even and ψ odd with respect to B_0 and B_L, and the contour C can be reduced

using the method of images. For long tanks ($L \gg 1$) it is numerically more efficient to use images about the bottom only and (3.2) is written as

$$2\pi i \beta(\zeta, t) = \int_{C'} \left[\frac{\beta(z,t)}{z-\zeta} - \frac{\beta^*(z,t)}{z^*-\zeta-2i} \right] dz, \tag{3.6}$$

where $C' = F \cup B \cup B_L$. If we now let ζ approach C', the real part of (3.6) for ζ on F and the imaginary part on $B \cup B_L$ yield respectively Fredholm integral equations of the second kind for ψ on F, and for ϕ on B and B_L (Vinje & Brevig 1981). The system can then be solved for the complete complex potential along the boundary.

For comparison to the fully nonlinear theory as well as the experiments, we also write down the linearized solution to the transient wavemaker problem. The linearized velocity potential $\bar{\phi}$ for a tank of length L can be expressed in a Fourier series as

$$\begin{aligned} \bar{\phi} = 2U(t) \sum_{m=0}^{\infty} \sin \kappa_m y \frac{\cosh \kappa_m (x-L)}{\kappa_m^2 \sinh \kappa_m L} \\ -\frac{4}{L} \sum_{n=1}^{\infty} \left[\sum_{m=0}^{\infty} (k_n^2 + \kappa_m^2)^{-1} \right] \frac{\cosh k_n (y+1) \cos k_n x}{\omega_n \cosh k_n} \\ \times \int_0^t d\tau\, U(\tau) \sin \omega_n (t-\tau) - \frac{1}{L} \int_0^t d\tau' \int_0^{\tau'} d\tau\, U(\tau), \end{aligned} \tag{3.7a}$$

where $\kappa_m = (m+\frac{1}{2})\pi, k_n = n\pi/L, \omega_n^2 = k_n \tanh k_n$, and the first and last two terms account respectively for the impulsive flow and the memory effect of the free surface. The corresponding linearized free-surface elevation $\bar{\eta}$ is

$$\bar{\eta} = \frac{4}{L} \sum_{n=1}^{\infty} \left[\sum_{m=0}^{\infty} (k_n^2 + \kappa_m^2)^{-1} \right] \cos k_n x \int_0^t d\tau\, U(\tau) \cos \omega_n (t-\tau) + \frac{1}{L} \int_0^t d\tau\, U(\tau), \tag{3.7b}$$

Equations (3.7) are the finite-length-tank Fourier-series form of the classical infinite-tank transient wavemaker solution of Kennard (1949).

4. Numerical implementation

To discretize (3.6), we (i) subdivide C' into linear segments, (ii) represent ϕ and ψ by linear basis functions over each segment, and (iii) collocate at selected points on C' corresponding to the end points of the segments. The resulting influence coefficients and their asymptotic approximations are given in Vinje & Brevig (1981). To avoid numerical difficulties due to the weak singularities at the intersections of the free surface with the tank walls we use Lin's (1984) technique and prescribe both the velocity potential ϕ and stream function ψ at these points by enforcing both the free-surface and body boundary conditions there. The resulting system of linear algebraic equations is amenable to iterative solutions (Baker, Meiron & Orszag 1982), although in practice even for $O(1000)$ unknowns the computation time is dominated by the calculation of the matrix elements themselves (which we do not vectorize well), and we simply use a vectorized Gaussian elimination scheme with partial pivoting to find the solution. Once the velocity potential and stream function are known everywhere on the fluid boundary, a second-order difference formula is used to find the velocities on the boundary. To calculate fluid velocities inside the contour, the most obvious choice is to take the derivative of (3.6) with respect to ζ. However, since the complex potential β is only piecewise linear, the influence coefficients of the

fluid velocity within a few panel lengths of the contour are logarithmically singular. A more robust and accurate method is to use the fluid velocity on the boundary contour, calculated by differencing, directly in Cauchy's integral to calculate the velocity inside the fluid:

$$2\pi i \frac{\partial \beta}{\partial z}(\zeta, t) = \int_{C'} \left[\frac{\frac{\partial \beta}{\partial z}(z, t)}{z - \zeta} - \frac{\frac{\partial \beta^*}{\partial z}(z, t)}{z^* - \zeta - 2i} \right] dz, \tag{4.1}$$

whose influence coefficients are non-singular as the field point ζ approaches the boundary C'.

For the integration of the free-surface boundary conditions (3.5), the fourth-order multi-step Adams–Bashforth–Moulton (ABM4) predictor–corrector method is used, and the fourth-order Runge–Kutta (RK4) technique is used to start the scheme (Longuet-Higgins & Cokelet 1976). A von Neumann stability analysis of the linearized problem shows that RK4 is conditionally stable for $\Delta t^2 \leqslant 8\Delta x/\pi$, where Δt is the time step and Δx is the minimum grid spacing. On the other hand, ABM4 is weakly unstable with a growth rate proportional to $\Delta t^6/\Delta x^3$. These linearized stability analyses are given in Appendix A. A stronger saw-tooth instability first reported by Longuet-Higgins & Cokelet (1976) is also observed by most investigators using the mixed-Eulerian–Lagrangian approach. The exact cause of this instability is not well understood, but we believe that one important mechanism is the concentration of Lagrangian points in regions of high velocity gradients where locally the wavenumbers are so high that small errors in the complex potential can cause large errors in the water-particle velocities. Thus, in order to minimize the highest wavenumbers, we adopt a regridding algorithm (Fink & Soh 1974; Dommermuth & Yue 1987) wherein a new set of equally spaced free-surface control points are selected after a fixed number of time steps. In our regridding calculations, we use quadratic interpolations for both the new surface positions and the potential values, which are found to conserve total energy as well as the five-point smoothing formula used by Longuet-Higgins & Cokelet (1976). Although both regridding and smoothing effectively remove high-wavenumber instabilities, smoothing cannot be applied as easily as regridding near the intersections of the free surface with the wavemaker and far wall. The main disadvantage of regridding is the loss of resolution near the cusp of a plunging wave where Lagrangian points would otherwise concentrate. Thus, when the wave is about to break, we switch to a five-point smoothing (except near the intersection of the free surface with the wavemaker and far wall) and reduce the time step accordingly. Interestingly, Baker *et al.* (1982), who used regridding to evaluate to high accuracy the integral equations which govern the motion of the interface between two fluids of different densities, also found it necessary to use smoothing.

Since the plunging phase of the wave is characterized by large velocities and disparate timescales, we use a dynamic time-stepping procedure whereby a new time step is chosen after each regridding or smoothing operation such that no panel moves more than 10% of its length in a given time step.

The accuracy and convergence of both the field-equation solver and the time-stepping procedure are checked independently against known (prescribed) solutions. Our numerical experiments indicate that when forty segments are used per wavelength, the average relative error of the discretized version of (3.7) is less than 0.5%, and the convergence with grid size is quadratic (see table 1). Similarly, the time-stepping procedure has less than 0.1% relative error when forty time steps per

wave period are used and the global truncation error is fourth order, as expected. In addition to these tests for convergence with respect to spatial and temporal discretizations, the overall accuracy of the numerical simulation is also evaluated for conserved total fluid volume and conservation of energy:

$$\int_B pU\,\mathrm{d}s = \frac{1}{2}\frac{\mathrm{d}}{\mathrm{d}t}\left[\int_{B\cup F}\phi\,\mathrm{d}\psi + \int_F y^2 n_y\,\mathrm{d}s\right] + \tfrac{1}{2}U. \tag{4.2}$$

The first term represents the power input by the wavemaker in terms of the total pressure p, and the second and last two terms represent respectively the rates of change of the kinetic and potential energies of the fluid. The $\frac{1}{2}U$ term represents the rate-of-change of potential energy associated with the changing length of the tank bottom with time. Here, n_y is the component of the unit outward-pointing normal in the vertical direction. To evaluate the accuracy of the numerical simulation, a better measure is obtained by eliminating the hydrostatic contribution ($\frac{1}{2}U$) from both sides of (4.2). Such checks are satisfied to within 1% up to wave plunging (see e.g. figure 5).

For the comparison with the single-plunging-wave experiment, we use a numerical tank of length 20 (corresponding to a length of 12 m for a physical tank depth of 0.6 m) with 500 linear segments on the free surface and 25 segments on the wavemaker and the far wall for a total of $N \approx 550$ unknowns. For this many unknowns, 80% of the computation time is devoted to the assembly of the influence coefficients, and the remaining 20% is dominated by the LU decomposition of the matrix solution. Altogether, about 4000 time steps are used to complete the simulation to the point where the plunger re-enters the free surface. Of these, we use regridding every 15 time steps for the first 3000 steps, and employ smoothing every 5 steps for the final 1000 steps. In the dynamic time-stepping procedure, the largest time step used is 0.08 at the beginning of the simulation and the smallest is 0.0004 near the end to capture the overturning wave. Consequently, more than half of the computational effort is used in the final 20% of the simulation time. The entire simulation uses 30 hours on a Cray 1 supercomputer, which is needed because a very fine resolution is sought, and also because the breaking event in the experiment occurs at a relatively large distance and time from the start of the wavemaker motion. In our simulation, approximately 7 wavelengths and 12 periods of the central wave component ($\omega_c = 1.4$) are modelled. The computational effort increases quadratically with the length of the tank and linearly with simulation time. If our error tolerance is doubled (see tables 1 and 2), or if the distance at wave plunging is halved, the computation time for the simulation can be reduced to a few hours.

5. Computational and experimental results

The velocity of the piston wavemaker is calculated by taking centred finite differences of the wavemaker displacement which is measured in the experiment. This velocity is the *only* input to the numerical simulation. The measured time history of the wavemaker velocity $U(t)$ is given as a Fourier-cosine series:

$$U(t) = \sum_{n=1}^{72} U_n \cos(\omega_n t - \theta_n), \tag{5.1}$$

where, to achieve about 3 significant figures of accuracy, 72 components are required. The amplitudes U_n, frequencies ω_n, and phases θ_n are tabulated in Appendix B.

ϵ	Panels/Wave	$\left\|\frac{\partial\beta}{\partial z}-\frac{\partial\tilde{\beta}}{\partial z}\right\|_{\max} \Big/ \left\|\frac{\partial\beta}{\partial z}\right\|_{\max}$
0.1	20	0.23×10^{-1}
	40	0.58×10^{-2}
	80	0.15×10^{-2}
	160	0.37×10^{-3}
0.3	20	0.23×10^{-1}
	40	0.58×10^{-2}
	80	0.15×10^{-2}
	160	0.37×10^{-3}
0.4	20	0.60×10^{-1}
	40	0.13×10^{-1}
	80	0.30×10^{-2}
	160	0.76×10^{-3}

TABLE 1. Maximum relative error in the free-surface velocity of a Stokes wave of (total) wave steepness ϵ for different numbers of panels per wave.

Total no. of panels	Δt	η (no regrid)	η (regrid)
100	0.10	−0.06361	−0.06361
150	0.075	−0.06675	−0.06624
200	0.075	−0.06611	−0.06582
250	0.050	−0.06610	−0.06621
Experiments	—	−0.0670	—

TABLE 2. Convergence of the surface elevation $\eta\,(x = 3.17, t = 25)$ as the number of panels increases and the time step is reduced. The tank length is $L = 8$. The panels are initially evenly distributed over the wavemaker, free surface and far wall.

To evaluate the accuracy and convergence of the scheme, we first test the convergence with panel length of our boundary-value problem solver for (3.2) using exact deep-water progressive Stokes waves as a benchmark. For the solution of the latter, we follow Schwartz (1974) but solve the nonlinear equations associated with the mapping function (Schwartz's equations 2.6) directly using Newton–Raphson iteration rather than high-order perturbation. The final results are exact to 10 significant figures. We prescribe the position of the free surface and the potential on it from the exact solution and solve for the stream function on the free surface numerically using a periodic extension of (3.2). The relative errors between the exact $(\partial\beta/\partial z)$ and calculated velocities $(\partial\bar{\beta}/\partial z)$ on the free surface are summarized in table 1 for a range of Stokes-wave steepnesses and panels per wavelength. As expected, for each wave steepness, the relative error decreases quadratically with panel size. From the harmonic content of the wavemaker velocity given in Appendix B, we see that most of the energy is concentrated below $\omega \sim 2$. Thus, by using 500 equally spaced panels distributed over the tank length, or approximately forty panels per wavelength, we are able to achieve a relative error of less than 0.5% for moderately steep waves ($\epsilon \leqslant 0.2$). As the wave nears overturning, switching to smoothing instead of regridding allows the panels to eventually become five times denser in regions of large gradients.

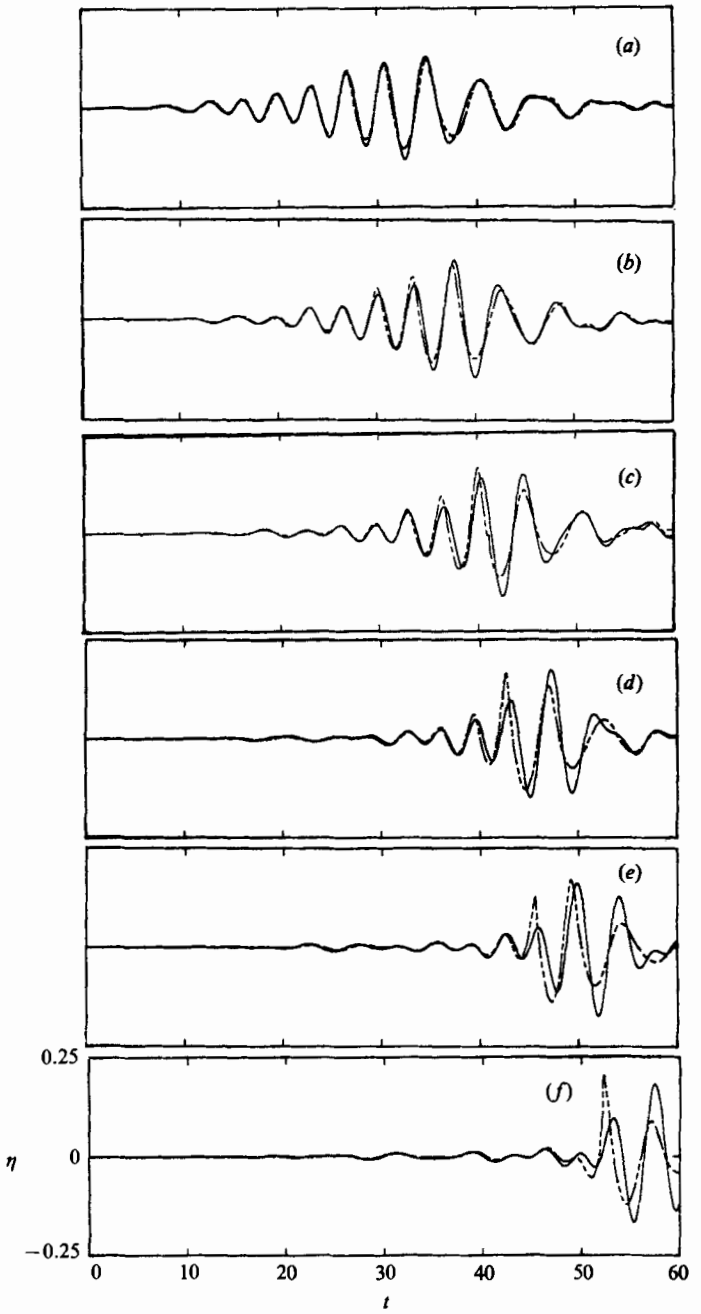

FIGURE 1. Free-surface elevations according to linearized theory (——) compared to wave-probe measurements (– – – –) as a function of time at distances from the wavemaker of (*a*) $x = 3.17$, (*b*) 5.00, (*c*) 6.67, (*d*) 8.33, (*e*) 10.00 and (*f*) 12.17.

The accuracy of our time-stepping procedure and of the overall problem is checked by systematically increasing the number of panels and reducing the time step for simulations of the plunging-breaker experiment. The measured and calculated free-surface elevations at a time midway to the breaking event are compared in table 2 for a tank of length $L = 8$. For 250 panels and $\Delta t = 0.05$, which roughly corresponds

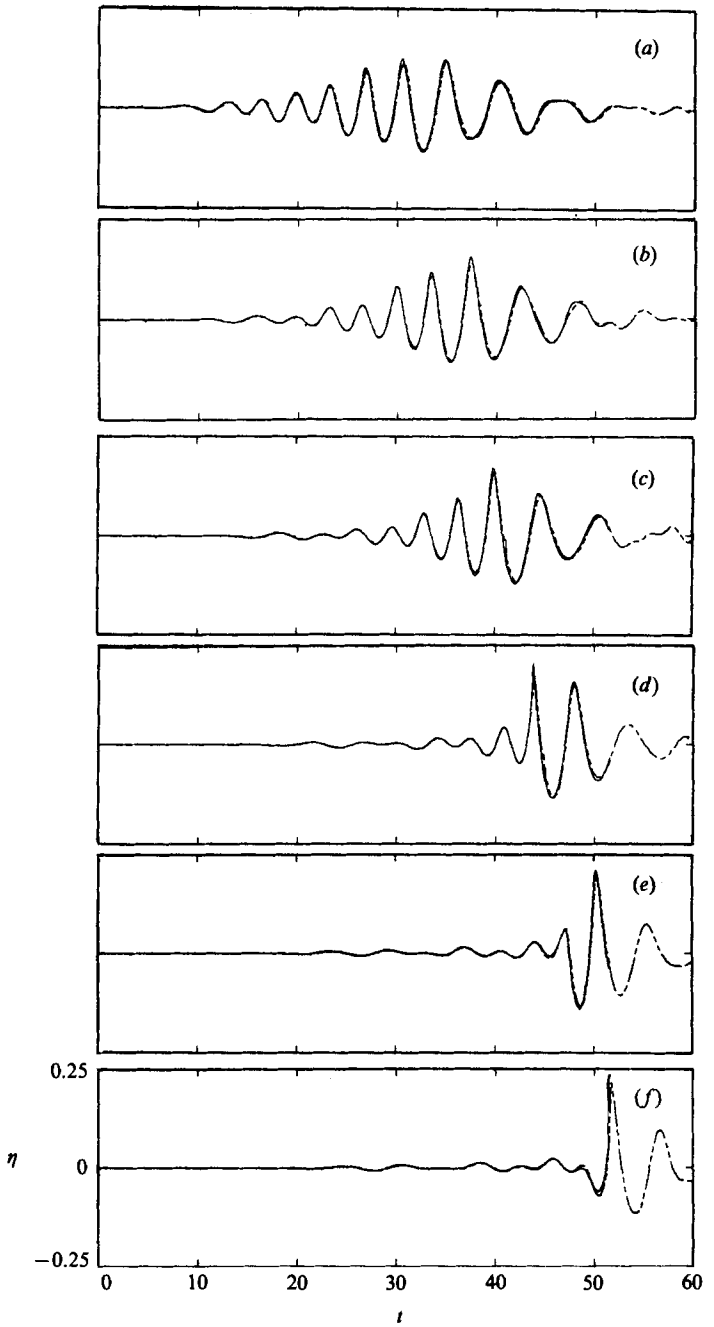

FIGURE 2. Free-surface elevations according to nonlinear theory (——) compared to wave-probe measurements (– – – –) as a function of time at distances from the wavemaker of (*a*) $x = 3.17$, (*b*) 5.00, (*c*) 6.67, (*d*) 9.17, (*e*) 10.83 and (*f*) 11.83.

to the computation parameters of our final simulation, the results have converged to within 0.02% with no regridding and 0.5% with regridding every 15 time steps. These errors are the same order of magnitude as those predicted in table 1 for the solution to the boundary-value problem alone.

The length of the tank used in our numerical simulation $L = 20$ is about 60% that

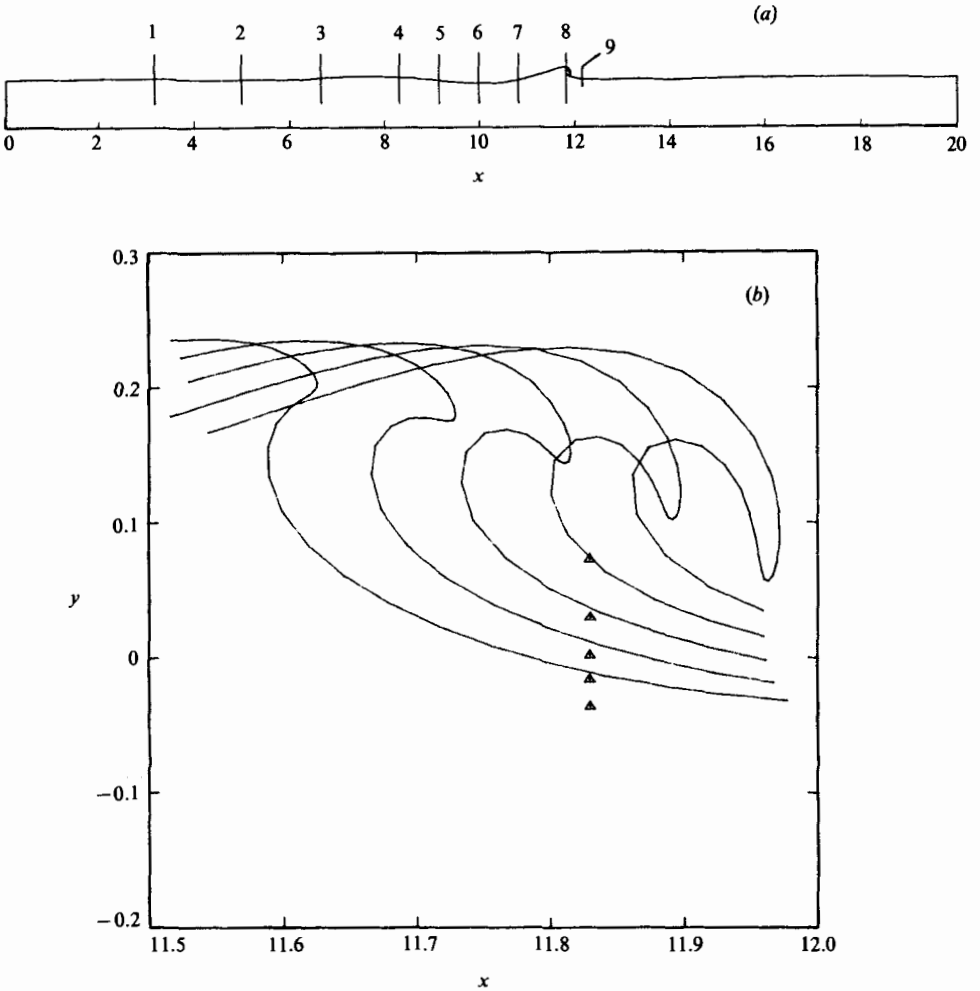

FIGURE 3. (*a*) Instantaneous free-surface profile of the simulated plunging wave at $t = 51.55$ showing the actual (undistorted) computational tank as well as the positions of the nine wave probes used in figures 1 and 2. (*b*) Details of the computed overturning wave (to scale) at times $t = 51.11$, 51.24, 51.34, 51.45 and 51.55 from left to right respectively. Symbols (△) represent wave-probe measurements at $x = 11.83$ (probe 8) at the same time instants from bottom to top respectively.

of the physical tank which, in addition, is equipped with an absorbing beach. To evaluate the effect of reflection from the far wall in the computations, the results according to linearized theory, (3.7), using the wavemaker velocity given by (5.1) are compared for two tank lengths corresponding to $L = 20$ and 40. Near the point where the wave plunges at $x = 12.2$, a harmonic analysis of the free-surface elevations indicates, as expected, that wave reflection is primarily limited to low wave frequencies, $\omega < 0.3$, and that the relative difference in energy between the two results is less than 2%. In view of the above, and to minimize computational effort, which increases roughly as $N^2 \sim L^2$, we use the shorter length of $L = 20$ for the nonlinear simulation.

In figure 1, the free-surface elevations according to *linearized* theory ($L = 20$) are compared to wave-probe measurements at $x = 3.17$, 5.00, 6.67, 8.33, 10.00 and 12.17.

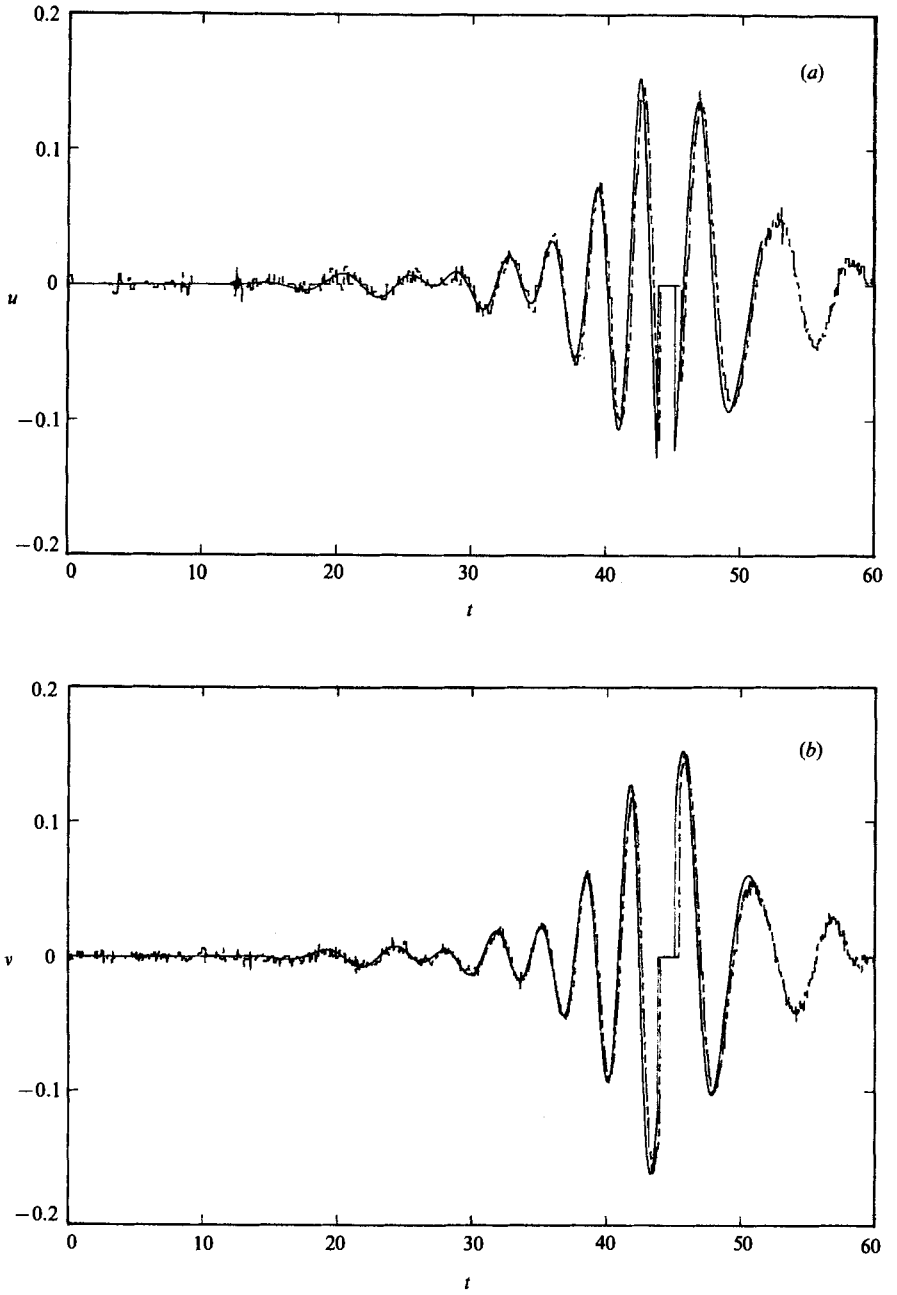

FIGURE 4(*a*, *b*). For caption see page 436.

The agreement becomes less satisfactory as the wave group steepens and travels down the tank. Near the plunging point the predicted linear wave amplitudes are in error by as much as 100% although the phases appear to agree somewhat better.

The comparisons between the surface elevations predicted by the *nonlinear* potential theory and those measured by wave probes at $x = 3.17$, 5.00, 6.67, 9.17, 10.83 and 11.83 are given in figure 2. Note that the nonlinear numerial simulation stops near $t = 52$ which is the time when the cusp of the plunging wave meets the

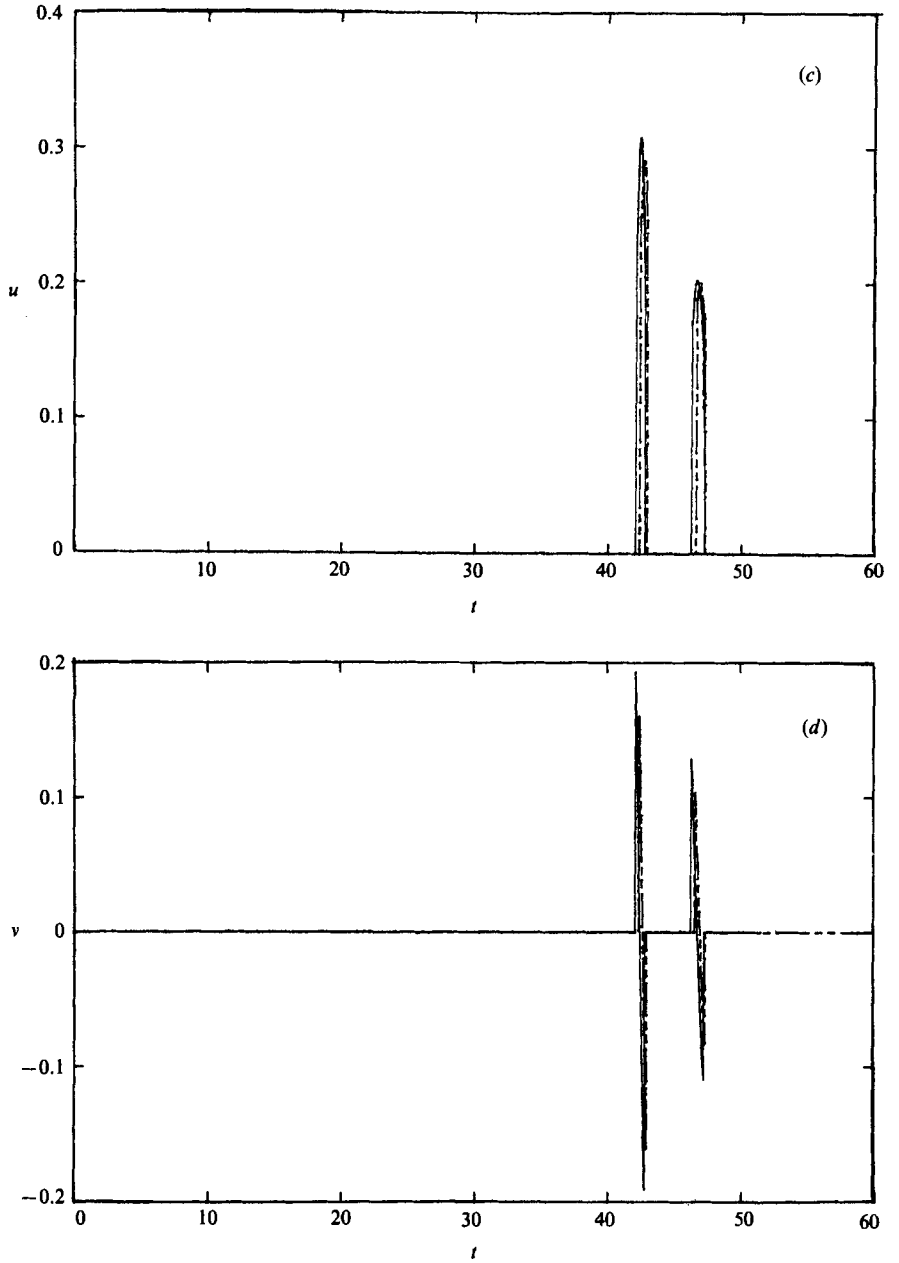

FIGURE 4(*c*,*d*). For caption see page 436.

wave trough in front (see figure 3). The computed and measured profiles can barely be distinguished up to the plunging location. For $x = 11.83$, the discrepancies are no greater than those discussed earlier when linear theory is applied to two tanks of different lengths, so that the errors in the nonlinear simulation may be partly attributed to wave reflection from the endwall of the computational tank.

In figure 3 we plot the computed instantaneous free-surface profiles near the plunging location at times $t = 51.11$, 51.24, 51.34, 51.45 and 51.55, which are compared to the wave-probe measurements at $x = 11.83$ taken at the same time

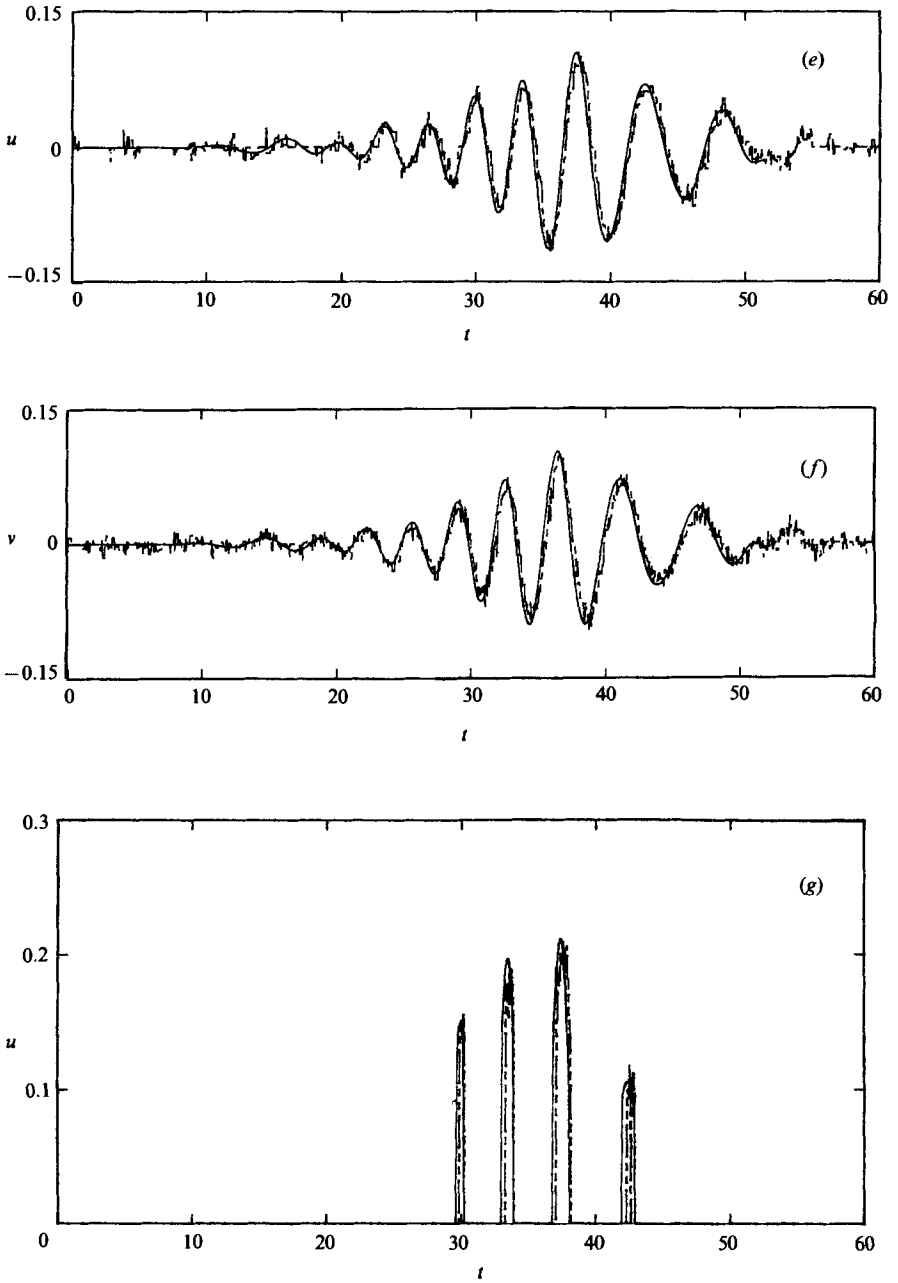

FIGURE 4. Water-particle velocities according to nonlinear theory (——) compared to measurements using a laser-Doppler anemometer (– – – –) as a function of time. (*a*) $u(8.33, -0.10, t)$; (*b*) $v(8.33, -0.10, t)$; (*c*) $u(8.33, 0.10, t)$; (*d*) $v(8.33, 0.10, t)$; (*e*) $u(5.00, -0.25, t)$; (*f*) $v(5.00, -0.25, t)$ and (*g*) $u(5.00, 0.067, t)$.

instants. (Note that the wave has not yet become multi-valued at the probe.) The nonlinear computations predict that the wave plunges closer to the wavemaker and at an earlier time than is observed. The deviations in the estimated plunging position and time are respectively $\Delta x \approx 0.15$ and $\Delta t \approx 0.25$. From the figure, the wave trough immediately in front of the breaker appears to rise faster and higher in

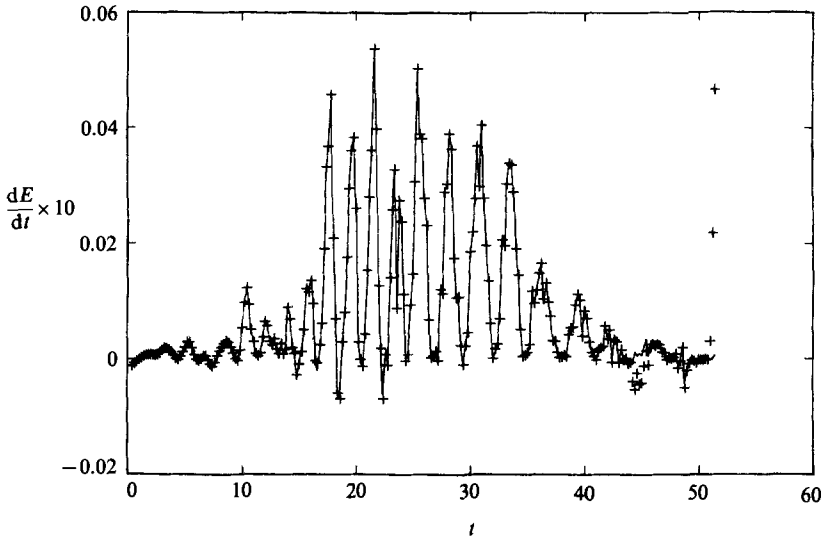

FIGURE 5. Energy conservation as a function of time: power input into the fluid by the wavemaker (——); and rate of change of total energy of the fluid in the tank (+). Note that the mean hydrostatic contribution is subtracted out.

the numerical simulation suggesting that some of the errors can be attributed to reflection from the far wall. Another possible effect is the presence of some (albeit small) dissipation in the physical experiment which tends to delay the breaking event. Given the large local velocities and accelerations of the plunging wave (see figure 6) the observed discrepancies are, however, within the expected accuracies of the computation and experiment.

As a final comparison, we examine the fluid-particle velocities measured using a laser-Doppler anemometer and the velocities computed using (4.1). Figure 4 shows these comparisons for the horizontal and vertical velocities $u(x_0, y_0, t)$ and $v(x_0, y_0, t)$ for horizontal positions located at $x_0 = 5$ and 8.33 over a range of vertical positions y_0. As before, the agreement is excellent. For points above the still-water level the velocity traces show intermittent pulses (positive for u and changing sign for v) which correspond to the passage of individual wave crests. When y_0 is below but close to the still-water level, the velocity curves may appear cut off at zero (truncated peaks for u and at upward zero-crossings for v) as the sample point comes out of the water at the troughs.

An advantage of a numerical simulation over a sequence of repeatable physical experiments is that useful information that requires difficult measurements such as *in situ* pressures or a large number of readings such as fluxes is now readily available. With the above validations of the computational results with respect to surface elevations and particle velocities, we proceed now to compute some quantities of special interest. Figure 5 shows the power input into the fluid by the wavemaker compared to the rate of change of the total energy of the fluid (see (4.2)). The global error of the numerical simulation with respect to energy conservation is less than a few percent for most of the simulation. Note that the discrepancy becomes noticeable after $t \sim 42$, which coincides with the time when numerical smoothing is introduced.

New *et al.* (1985) examined the velocities and accelerations of particles in the free surface of periodic overturning waves on finite (shallow) depth and observed maximum horizontal velocities almost twice the linear phase speed and maximum

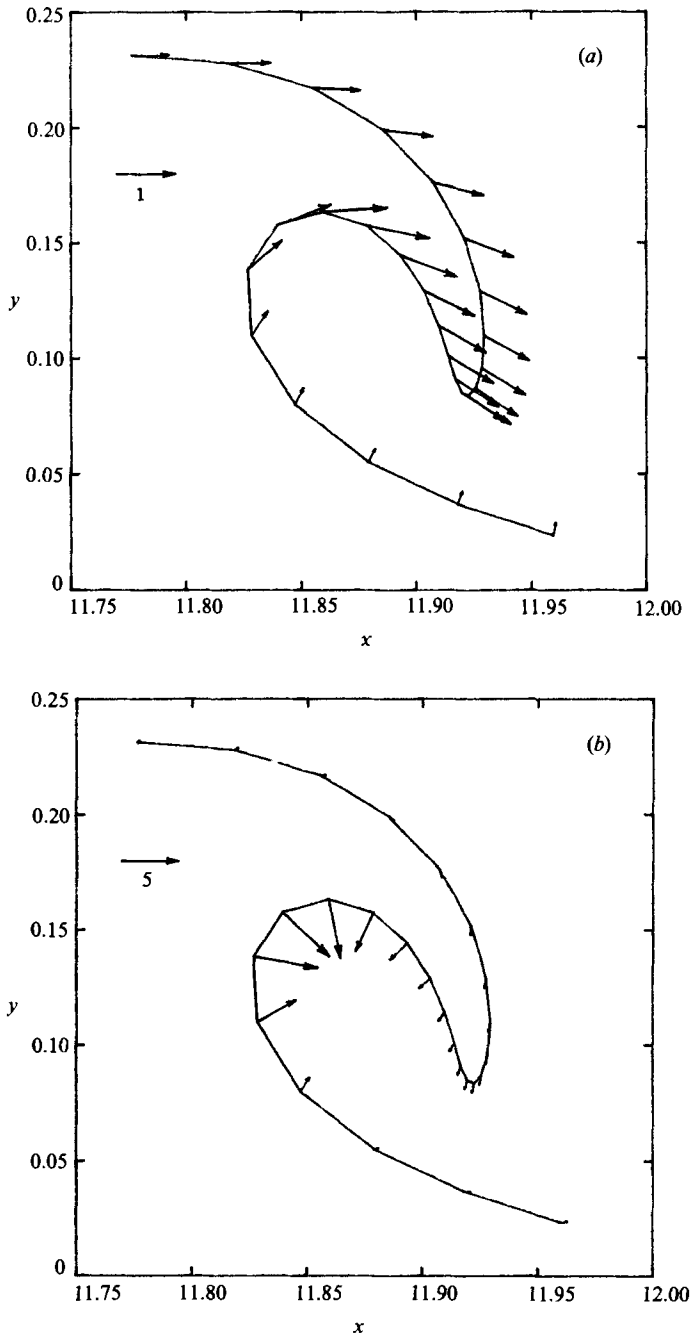

FIGURE 6. (*a*) Vector velocities and (*b*) Lagrangian accelerations of fluid surface particles of the deep-water plunging breaker at time $t = 51.5$ just before re-entry occurs.

accelerations up to six times that of gravity. It is of interest to examine these quantities in the present case of deep-water breaking waves created by the superposition of a spectrum of waves whose phases have been judiciously chosen. The vector velocities and accelerations of surface particles at time $t = 51.5$ just before re-entry are shown in figure 6. The maximum velocity amplitude occurs in the cusp of

the wave and is roughly twice as large as the linear phase speed based on a central frequency of $\omega_c \approx 1.4$. The maximum Lagrangian accelerations, which occur inside the loop, are of the order of $6g$ and are directed radially inward. In the cusp of the wave the maximum acceleration is approximately g and is directed downward so that the tip of this overhanging wave is essentially in free fall. The resemblance of the kinematics of the deep-water plunging wave in the present case and that of the periodic shallow-water overturning wave computed by New *et al.* (1985), as well as that created by an asymmetrically applied surface pressure (Longuet-Higgins & Cokelet 1976), is quite remarkable. This further confirms New *et al.*'s conjecture that the evolution of an overturning wave must be relatively independent of the interior dynamics, so that a local solution for the jet (Longuet-Higgins 1982; New 1983; Greenhow 1983) may be surprisingly useful.

6. Conclusion

High-resolution state-of-the-art experiments and computations have been carried out to study steep and overturning gravity waves produced by a piston wavemaker in a tank. The comparisons between measurements and fully nonlinear potential-theory computations for a plunging breaker are found to be excellent for the surface elevations, and horizontal and vertical velocities at various depths. This confirms the validity and usefulness of potential-theory calculations for such waves and that other physical mechanisms must play a very minor role up to the point of wave re-entry. Although much work remains to be done to improve the efficiency and robustness of nonlinear free-surface potential-flow calculations, especially in the treatment of open boundaries (e.g. the use of matching radiation boundaries by Dommermuth & Yue 1987), the present work is an important step towards establishing their usefulness, limitations, and applications in ocean science and engineering.

This research was supported by the National Science Foundation (NSF Grant MEA 8514919) and the Office of Naval Research (Contract N00014-82-K-0198). Most of the computations were performed at the NSF sponsored Minnesota Supercomputer Institute. The authors would like to thank Professor J. N. Newman for suggesting this collaboration between theory and experiments, and for his encouragement during this research.

Appendix A. Linearized von Neumann stability analysis

Let ϕ^k and η^k be the Fourier modal amplitudes at time $t = k\Delta t$ of the potential and surface elevation respectively of a deep-water Airy wave. If, for simplicity, we assume that ϕ and η are normalized such that the frequency and wavenumber are one, then the linearized free-surface boundary conditions are simply

$$\begin{Bmatrix} \phi_t^k \\ \eta_t^k \end{Bmatrix} = \begin{Bmatrix} -\eta^k \\ \phi^k \end{Bmatrix}. \tag{A 1}$$

Thus, ϕ^k and η^k can be expressed exactly in terms of their initial values ϕ^0 and η^0 by the transformation (or amplification) matrix $\boldsymbol{T}$:

$$\begin{Bmatrix} \phi^k \\ \eta^k \end{Bmatrix} = \boldsymbol{T}^k \begin{Bmatrix} \eta^0 \\ \phi^0 \end{Bmatrix} \equiv \begin{bmatrix} \cos(\Delta t) & -\sin(\Delta t) \\ \sin(\Delta t) & \cos(\Delta t) \end{bmatrix}^k \begin{Bmatrix} \phi^0 \\ \eta^0 \end{Bmatrix}. \tag{A 2}$$

Note that (A 2) is neutrally stable since the exact matrix $\boldsymbol{T}$ has a spectral radius of unity. In a numerical time integrator, $\boldsymbol{T}$ is replaced by some approximation, say $\tilde{\boldsymbol{T}}$, and the scheme is conditionally stable if its spectral radius is less than or equal to one for some suitably small value of Δt; neutrally stable if it is exactly one; and unstable if it is greater than one.

For example, for any of the explicit fourth-order Runge–Kutta methods (RK4), direct substitution into (A 1) gives

$$\tilde{\boldsymbol{T}} = \begin{bmatrix} 1-\frac{\Delta t^2}{2}+\frac{\Delta t^4}{24} & -\Delta t+\frac{\Delta t^3}{6} \\ \Delta t-\frac{\Delta t^3}{6} & 1-\frac{\Delta t^2}{2}+\frac{\Delta t^4}{24} \end{bmatrix}, \tag{A 3}$$

which is simply the fourth-order Taylor-series expansion of the exact transformation matrix $\boldsymbol{T}$ defined in (A 2). The magnitudes of the eigenvalues of this matrix are less than or equal to one if $\Delta t^2 \leqslant 8$, which is the Courant condition for the stability of RK4. Furthermore, for $\Delta t \ll 1$, the r.m.s. norm of the vector $\{\phi^k, \eta^k\}$ attenuates like $(1-\Delta t^6/144)^k$ to leading order so that, in fact, RK4 is mildly dissipative.

Substituting the fourth-order multi-step Adams–Bashforth–Moulton predictor–corrector method (ABM4) into (A 1), we obtain an algebraic equation for $\tilde{\boldsymbol{T}}$:

$$\tilde{\boldsymbol{T}}^4 - \begin{bmatrix} 1-\frac{55\Delta t^2}{64} & -\frac{7\Delta t}{6} \\ \frac{7\Delta t}{6} & 1-\frac{55\Delta t^2}{64} \end{bmatrix} \tilde{\boldsymbol{T}}^3 - \begin{bmatrix} \frac{59\Delta t^2}{64} & \frac{5\Delta t}{24} \\ -\frac{5\Delta t}{24} & \frac{59\Delta t^2}{64} \end{bmatrix} \tilde{\boldsymbol{T}}^2$$
$$- \begin{bmatrix} -\frac{37\Delta t^2}{64} & -\frac{\Delta t}{24} \\ \frac{\Delta t}{24} & -\frac{37\Delta t^2}{64} \end{bmatrix} \tilde{\boldsymbol{T}} - \begin{bmatrix} \frac{9\Delta t^2}{64} & 0 \\ 0 & \frac{9\Delta t^2}{64} \end{bmatrix} = 0. \tag{A 4}$$

For $\Delta t \ll 1$, $\tilde{\boldsymbol{T}}$ may be expanded in a perturbation series in Δt, $\tilde{\boldsymbol{T}} = \tilde{\boldsymbol{T}}^{(0)} + \Delta t\, \tilde{\boldsymbol{T}}^{(1)} + \Delta t^2\, \tilde{\boldsymbol{T}}^{(2)} + \ldots$, which when substituted into (A 4) can be solved at each order to yield finally

$$\tilde{\boldsymbol{T}} = \begin{bmatrix} 1-\frac{\Delta t^2}{2}+\frac{\Delta t^4}{24}+\frac{77\Delta t^6}{576}+O(\Delta t^8) & -\Delta t+\frac{\Delta t^3}{6}-\frac{5\Delta t^5}{144}+O(\Delta t^7) \\ \Delta t-\frac{\Delta t^3}{6}+\frac{5\Delta t^5}{144}+O(\Delta t^7) & 1-\frac{\Delta t^2}{2}+\frac{\Delta t^4}{24}+\frac{77\Delta t^6}{576}+O(\Delta t^8) \end{bmatrix}. \tag{A 5}$$

Since the magnitudes of the eigenvalues of this matrix are greater than one, ABM4 is strictly unstable. The instability is quite weak ($O(\Delta t^6)$), however, and the r.m.s. norm of $\{\phi^k, \eta^k\}$ grows only as $(1+31\Delta t^6/192)^k$ to leading order.

Appendix B. Fourier-cosine coefficients of the wave-paddle velocity

The following Fourier-cosine series frequencies ω_n, amplitudes U_n, and phases θ_n of (5.1) approximates the measured time history of the wave-paddle velocity. These data are used as input in the numerical simulation.

n	ω_n	U_n	θ_n	n	ω_n	U_n	θ_n
1	0.1519	0.5654×10^{-4}	3.0297	2	0.2279	0.9869×10^{-4}	0.1389
3	0.3038	0.1377×10^{-3}	−2.1163	4	0.3798	0.1527×10^{-3}	1.3747
5	0.4558	0.2450×10^{-3}	−0.9151	6	0.5317	0.2545×10^{-3}	2.8300
7	0.6077	0.4459×10^{-3}	0.2571	8	0.6836	0.4492×10^{-3}	−2.0714
9	0.7596	0.8974×10^{-3}	1.4644	10	0.8356	0.1541×10^{-2}	−0.3737
11	0.9115	0.6153×10^{-2}	2.4358	12	0.9875	0.9238×10^{-2}	−1.3082
13	1.0635	0.9940×10^{-2}	1.4715	14	1.1394	0.1154×10^{-1}	−2.1312
15	1.2154	0.1119×10^{-1}	0.2868	16	1.2913	0.1107×10^{-1}	2.5881
17	1.3673	0.1252×10^{-1}	−1.6385	18	1.4433	0.1266×10^{-1}	0.2799
19	1.5192	0.1222×10^{-1}	2.1047	20	1.5952	0.1364×10^{-1}	−2.5568
21	1.6711	0.1455×10^{-1}	−1.1489	22	1.7471	0.1392×10^{-1}	0.0107
23	1.8231	0.1238×10^{-1}	1.2493	24	1.8990	0.5689×10^{-2}	2.6881
25	1.9750	0.1080×10^{-2}	1.9636	26	2.0509	0.1058×10^{-2}	2.9378
27	2.1269	0.9421×10^{-3}	2.2129	28	2.2029	0.2670×10^{-3}	2.7790
29	2.2788	0.6281×10^{-3}	2.6601	30	2.3548	0.3360×10^{-3}	1.7339
31	2.4307	0.3658×10^{-3}	3.0376	32	2.5067	0.4146×10^{-3}	2.2011
33	2.5827	0.7860×10^{-4}	−3.1064	34	2.6586	0.3672×10^{-3}	2.6224
35	2.7346	0.1616×10^{-3}	1.4726	36	2.8105	0.2907×10^{-3}	3.1352
37	2.8865	0.2440×10^{-3}	1.8683	38	2.9625	0.1448×10^{-3}	−2.8378
39	3.0384	0.2539×10^{-3}	2.3050	40	3.1144	0.9563×10^{-4}	−2.9911
41	3.1904	0.5133×10^{-4}	2.3894	42	3.2663	0.2960×10^{-3}	2.1860
43	3.3423	0.1549×10^{-3}	−1.9536	44	3.4182	0.2719×10^{-3}	1.8677
45	3.4942	0.1825×10^{-3}	−2.8750	46	3.5702	0.3097×10^{-4}	−1.9432
47	3.6461	0.2818×10^{-3}	1.7837	48	3.7221	0.2959×10^{-3}	−2.6032
49	3.7980	0.1226×10^{-3}	0.9362	50	3.8740	0.1698×10^{-3}	2.5802
51	3.9500	0.1780×10^{-3}	−2.9200	52	4.0259	0.4430×10^{-4}	−0.0013
53	4.1019	0.9739×10^{-4}	2.3082	54	4.1778	0.1568×10^{-3}	2.7947
55	4.2538	0.1163×10^{-3}	−1.4878	56	4.3298	0.1725×10^{-3}	1.8697
57	4.4057	0.1759×10^{-3}	−3.1163	58	4.4817	0.1729×10^{-3}	−1.6396
59	4.5576	0.2447×10^{-3}	0.8967	60	4.6336	0.2910×10^{-3}	2.6254
61	4.7096	0.2248×10^{-3}	−2.5408	62	4.7855	0.2095×10^{-3}	−0.7237
63	4.8615	0.2514×10^{-3}	1.4337	64	4.9375	0.3096×10^{-3}	2.7748
65	5.0134	0.3029×10^{-3}	−2.1868	66	5.0894	0.1904×10^{-3}	−0.6301
67	5.1653	0.1961×10^{-3}	1.0234	68	5.2413	0.2321×10^{-3}	2.4319
69	5.3173	0.1650×10^{-3}	3.0634	70	5.3932	0.2289×10^{-3}	−2.3772
71	5.4692	0.1056×10^{-3}	−1.8554	72	5.5451	0.6005×10^{-4}	−0.7142

REFERENCES

Baker, G. R., Meiron, D. I. & Orszag, S. A. 1982 Generalized vortex methods for free-surface flow problems. *J. Fluid Mech.* **123**, 477–501.

Chan, E. S. 1985 Deep water breaking wave forces on structures. Sc.D. dissertation, MIT, Dept. of Civil Engineering.

Dommermuth, D. G. & Yue, D. K. P. 1987 Numerical simulations of nonlinear axisymmetric flows with a free surface. *J. Fluid Mech.* **178**, 195–219.

Fink, P. T. & Soh, W. K. 1974 Calculation of vortex sheets in unsteady flow and applications in ship hydrodynamics. In *Proc. 10th Symp. Naval Hydro., Cambridge, MA* (ed. R. D. Cooper & S. W. Doroff), pp. 463–491. Washington: Government Printing Office.

GREENHOW, M. 1983 Free-surface flows related to breaking waves. *J. Fluid Mech.* **134**, 259–275.

GREENHOW, M., VINJE, T., BREVIG, P. & TAYLOR, J. 1982 A theoretical and experimental study of the capsize of Salter's duck in extreme waves. *J. Fluid Mech.* **118**, 221–239.

KENNARD, E. H. 1949 Generation of surface waves by a moving partition. *Q. Appl. Maths* **7**, 303–312.

LIN, W. M. 1984 Nonlinear motion of the free surface near a moving body. Ph.D. thesis, MIT, Dept. of Ocean Engineering.

LIN, W. M., NEWMAN, J. N. & YUE, D. K. P. 1984 Nonlinear forced motions of floating bodies. In *Proc. 15th Symp. on Naval Hydro., Hamburg*, pp. 33–49. Washington: National Academy Press.

LONGUET-HIGGINS, M. S. 1974 Breaking waves in deep or shallow water. In *Proc. 10th Symp. Naval Hydro., Cambridge, MA* (ed. R. D. Cooper & S. W. Doroff), pp. 597–605. Washington: Government Printing Office.

LONGUET-HIGGINS, M. S. 1982 Parametric solutions for breaking waves. *J. Fluid Mech.* **121**, 403–424.

LONGUET-HIGGINS, M. S. & COKELET, E. D. 1976 The deformation of steep surface waves on water. I. A numerical method of computation. *Proc. R. Soc. Lond.* A **350**, 1–26.

MELVILLE, W. K. & RAPP, R. J. 1985 Momentum flux in breaking waves. *Nature* **317**, 514–516.

NEW, A. 1983 A class of elliptical free-surface flows. *J. Fluid Mech.* **130**, 219–239.

NEW, A. L., MCIVER, P. & PEREGRINE, D. H. 1985 Computations of overturning waves. *J. Fluid Mech.* **150**, 233–251.

RAPP, R. J. 1986 Laboratory measurements of deep water breaking waves. Ph.D. thesis, MIT, Dept. of Ocean Engineering.

SCHWARTZ, L. W. 1974 Computer extension and analytic continuation of Stokes' expansion for gravity waves. *J. Fluid Mech.* **62**, 553–578.

URSELL, F., DEAN, R. G. & YU, Y. S. 1959 Forced small-amplitude water waves: a comparison of theory and experiment. *J. Fluid Mech.* **7**, 33–52.

VINJE, T. & BREVIG, P. 1981 Nonlinear ship motions. In *Proc. 3rd Intl Conf. Num. Ship Hydro., Paris*, pp. 257–268. Bassin d'Essais des Carènes, France.